Chapter 6
In-Situ Observation of the Formation of Laser-Induced Periodic Surface Structures with Extreme Spatial and Temporal Resolution

Klaus Sokolowski-Tinten, Jörn Bonse, Anton Barty, Henry N. Chapman, Saša Bajt, Mike J. Bogan, Sebastien Boutet, Andrea Cavalleri, Stefan Düsterer, Matthias Frank, Janos Hajdu, Stefan Hau-Riege, Stefano Marchesini, Nikola Stojanovic, and Rolf Treusch

Abstract Irradiation of solid surfaces with intense ultrashort laser pulses represents a unique way of depositing energy into materials. It allows to realize states of extreme electronic excitation and/or very high temperature and pressure and to drive materials close to and beyond fundamental stability limits. As a consequence, structural changes and phase transitions often occur along unusual pathways and under strongly nonequilibrium conditions. Due to the inherent multiscale nature—both temporally and spatially—of these *irreversible* processes, their direct experimental observation requires techniques that combine high temporal resolution with the appropriate spatial resolution and the capability to obtain good quality data on a single pulse/event basis. In this respect, fourth-generation light sources, namely, short wavelength and short pulse free electron lasers (FELs), are offering new and fascinating possibilities. As an example, this chapter will discuss the results of scattering experiments carried out at the FLASH free electron laser at DESY (Hamburg, Germany), which allowed us to resolve laser-induced structure formation at surfaces on the nanometer to submicron length scale and in temporal regimes ranging from picoseconds to several nanoseconds with sub-picosecond resolution.

Keywords Laser-induced periodic surface structures (LIPSS) · Capillary waves · Time-resolved scattering · Pump-probe experiments · Free electron laser

---

K. Sokolowski-Tinten (✉)
Faculty of Physics and Centre for Nanointegration Duisburg-Essen, University of Duisburg-Essen, Duisburg, Germany
e-mail: klaus.sokolowski-tinten@uni-due.de

J. Bonse
Bundesanstalt für Materialforschung und –prüfung (BAM), Berlin, Germany
e-mail: joern.bonse@bam.de

1   Introduction

Irradiation of solid surfaces with intense ultrashort laser pulses represents a unique way of depositing energy into materials. It allows to realize states of extreme electronic excitation and/or very high temperature and pressure and to drive materials close to and beyond fundamental stability limits. As a consequence, structural changes and phase transitions often occur along unusual pathways and under strongly nonequilibrium conditions [1].

Moreover, such laser-solid interactions at high intensities and fluences are not only interesting from a fundamental physics point of view but represent also the basis for numerous applications of lasers for materials processing and synthesis (e.g., see Part 3 of this book and references therein). In this general context, the formation of so-called **l**aser-**i**nduced **p**eriodic **s**urface **s**tructures (LIPSS) or ripples

A. Barty · S. Düsterer · R. Treusch
Deutsches Elektronen-Synchrotron DESY, Hamburg, Germany
e-mail: anton.barty@desy.de; stefan.duesterer@desy.de; rolf.treusch@desy.de

H. N. Chapman
Center for Free-Electron Laser Science CFEL, Deutsches Elektronen-Synchrotron DESY, Hamburg, Germany

Department of Physics, Universität Hamburg, Hamburg, Germany

The Hamburg Centre for Ultrafast Imaging, Hamburg, Germany
e-mail: henry.chapman@cfel.de

S. Bajt
Center for Free-Electron Laser Science CFEL, Deutsches Elektronen-Synchrotron DESY, Hamburg, Germany

The Hamburg Centre for Ultrafast Imaging, Hamburg, Germany
e-mail: sasa.bajt@desy.de

M. J. Bogan · M. Frank · S. Hau-Riege
Lawrence Livermore National Laboratory, Livermore, CA, USA
e-mail: mbogan@tractionondemand.com; frank1@llnl.gov; hauriege1@llnl.gov

S. Boutet · S. Marchesini
SLAC National Accelerator Laboratory, Menlo Park, CA, USA
e-mail: sboutet@slac.stanford.edu; smarches@slac.stanford.edu

A. Cavalleri
Max Planck Institute for the Structure and Dynamics of Matter, Hamburg, Germany
e-mail: andrea.cavalleri@mpsd.mpg.de

J. Hajdu
Department of Cell and Molecular Biology, Uppsala Universitet, Uppsala, Sweden

The European Extreme Light Infrastructure, Institute of Physics, Academy of Sciences of the Czech Republic, Dolní Břežany, Czech Republic
e-mail: janos.hajdu@icm.uu.se

N. Stojanovic
Deutsches Zentrum für Luft- und Raumfahrt (DLR) Berlin-Adlersdorf, Berlin, Germany
e-mail: nikola.stojanovic@dlr.de

represent an interesting and very common case under typical processing conditions, namely, irradiation of *real* (i.e., rough) surfaces with multiple/many pulses.

LIPSS have been first reported in 1965 by Birnbaum [2] on semiconductors irradiated with pulses from a free-running ruby laser ($\approx 200\,\mu s$ duration). Since then the topic has attracted continuous interest, not only to understand the basic mechanisms that lead to these sub-micrometer to nanoscale surface modifications, but also because LIPSS are considered as a versatile tool to achieve nanoscale structuring/patterning and functionalization of surfaces for a variety of applications (see [3] and references therein, as well as Chap. 23 of this book by Mezera et al.).

LIPSS have been observed on almost all kinds of materials and with any kind of laser. Depending on the LIPSS periodicity, different mechanisms are discussed in the very extensive literature. Meanwhile accepted is the view that LIPSS with a periodicity of the order of the laser wavelength (so-called low spatial frequency LIPSS: LSFL) can be attributed to the interference between the incident laser wave and waves scattered/excited at the surface leading to an intensity modulation and thus to a (periodically) modulated energy deposition [4]. In 1983, Sipe et al. [5] have developed this picture into a rigorous electromagnetic model which is frequently used and has been further developed since then [6–8].

More recently and so far only after irradiation with multiple ultrashort laser pulses, LIPSS with a periodicity much smaller than the laser wavelength have been observed. The mechanisms which lead to these high spatial frequency LIPSS (HSFL) are not fully clear yet. HSFL have been, for example, attributed to near-field scattering and interference effects [9] in conjunction with surface second harmonic generation (e.g., [6, 10, 11]), but also self-organization processes have been proposed [12, 13]. Very recently, a coupled electromagnetic-hydrodynamic mechanism was proposed, where thermocapillary melt flows (Marangoni convection instability) that are initiated by spatial gradients caused by polarization-dependent absorption at random nanobumps and nanoholes cause the formation of HSFL [14].

However, it is not the purpose of this contribution to discuss in detail all models and controversies about LIPSS (for reviews of the current understanding, the reader is referred to [15–17] and references therein), but to reveal and emphasize the *dynamical* aspects of LIPSS formation. In the vast majority of published work, LIPSS have been studied *post mortem* through an analysis of the permanent modifications of the irradiated surface. A comparatively small number of time-resolved experiments addressing both, the nanosecond [18–22] and the femtosecond and picosecond time range [23–29], have been performed. Using optical probing, direct imaging [24–29] and diffraction/scattering techniques [18–23] have been applied. However, the spatial resolution was limited by the optical probe wavelength which made it difficult/impossible to follow the transient structural evolution of the laser-irradiated surface on sub-micrometer to nanometer length scales. For a more general discussion on time-resolved optical probing, the reader is referred to Chap. 7 (M. Garcia-Lechuga et al.) of this book.

Here we present results of time-resolved scattering experiments performed at the extreme ultraviolet (XUV) free electron laser (FEL) FLASH at DESY in Hamburg (Germany) [30]. The unique combination of short wavelength, ultrashort pulse

duration, and high photon flux has opened up new and exciting possibilities since it allows the investigation of *irreversible* processes with high temporal resolution and the appropriate nanoscale spatial resolution. We make use of these possibilities to study in the time domain the formation of LIPSS at the surface of laser-excited thin silicon films.[1]

2 Time-Resolved XUV Scattering at FLASH

The FLASH free electron laser at DESY (Hamburg/Germany) was the first FEL operating at wavelengths below 50 nm [30]. It has been available to users since 2005 serving a broad scientific community interested in atomic, molecular, and cluster physics, high-energy-density research, dynamics at surfaces and diffraction imaging with high spatial resolution (see [32, 33] and references therein).

To address the particular topic of this contribution, namely, the dynamics of nanoscale structure formation at laser-irradiated surfaces, we carried out a series of time-resolved laser pump XUV scattering probe experiments to follow the laser-induced changes with femtosecond temporal and nanometer spatial resolution. A schematic of the experimental setup is shown in Fig. 6.1.

Experiments were performed at beamline BL2 [34], and FLASH was operated in the single-bunch ultrashort-pulse mode, providing pulses at a wavelength of 13.5 nm, a pulse duration of 10–20 fs and a mean pulse energy of about 20 μJ (corresponding to $> 10^{12}$ XUV photons per pulse). These pulses were focused onto
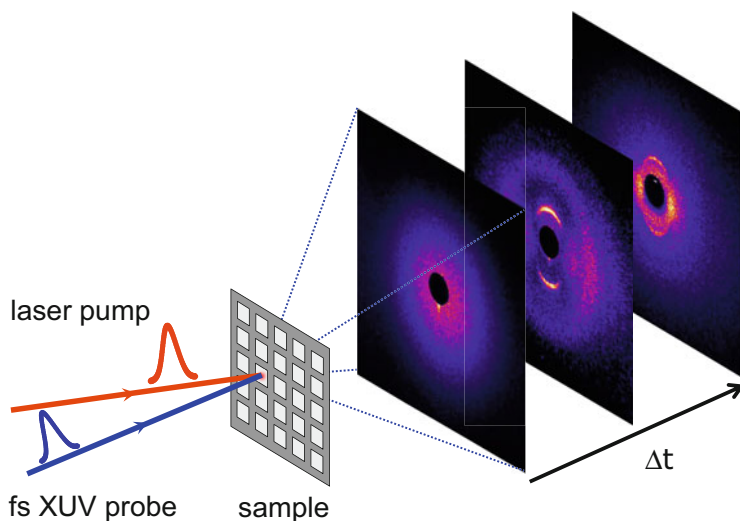

Fig. 6.1 Schematic of the time-resolved single-pulse scattering experiment performed at the XUV free electron laser FLASH

---

[1] Some of these results have been presented earlier in [31].

the sample under study (see below) to a spot size of approximately $20\,\mu m$ full width at half maximum (FWHM).

Scattering experiments were carried out in a normal-incidence transmission geometry. A 45° graded multilayer mirror with a central hole was used to selectively collect the radiation scattered by the sample and direct it onto a XUV-sensitive CCD detector while blocking at the same time any background scattering, plasma emission from the target, etc., as well as the direct beam (which passed through the central hole). At $\lambda_{XUV} = 13.5\,nm$, this diffraction setup allowed to measure scattering patterns over a spatial frequency range (spatial frequency $q = (2\pi/\lambda_{XUV}) \cdot sin(\theta)$; θ diffraction angle) from $\pm 10\,\mu m^{-1}$ (determined by the size of the central hole) to $\pm 110\,\mu m^{-1}$ (detector size), providing an effective spatial resolution of better than 50 nm [35]. For further details, the reader is referred to [36, 37].

Samples comprised polycrystalline silicon films with 100 nm thickness deposited onto arrays of free-standing, 20-nm-thick Si_3N_4 membranes supported by a silicon wafer frame. Such target arrays allowed replacement of the sample between consecutive exposures, because single-pulse irradiation with both, the optical laser and the FEL, leads to irreversible sample modifications (e.g., its destruction).

These samples have been irradiated with 12 ps, 523 nm laser pulses [38] at an angle of incidence of 47° (normally p-polarized) and an incident fluence of about $1.7\,J/cm^2$ (pump beam size on the sample $30 \times 40\,\mu m^2$ FWHM), well above the ablation threshold of $\lesssim 0.5\,J/cm^2$. The delay time Δt between the optical pump and the XUV probe was varied over a range from -50 ps to 4.5 ns with a help of a mechanical delay line.

For each delay time, three to five diffraction images have been recorded (each on a fresh sample window), and the data were averaged to increase the signal-to-noise ratio. Frequently, detector images without pump and probe, pump only, and probe only have been recorded to allow for background correction as well as to characterize the scattering of the non-excited samples.

3 Experimental Results

As first results, we present here data obtained on a 100-nm-thick polycrystalline silicon film, deposited on $100 \times 100\,\mu m^2$ sized Si_3N_4 membrane windows. Figure 6.2 shows a sequence of transient scattering patterns for different pump-probe delay times. The intensity scale of the false-color representation is in arbitrary units, but the same for all frames/delays. The black disk in the center of each image represents the "beam stop" realized by the hole in the XUV multilayer mirror. The projection of the pump laser beam polarization (p-pol.) onto the sample surface is indicated by the vertical solid white bar in the first frame of Fig. 6.2.

Before discussing the temporal evolution of these scattering patterns, we want to emphasize their "grainy" structure, which represent speckles due to the spatially coherent XUV illumination. From the average speckle size $\delta q_S \approx 0.4\,\mu m^{-1}$,
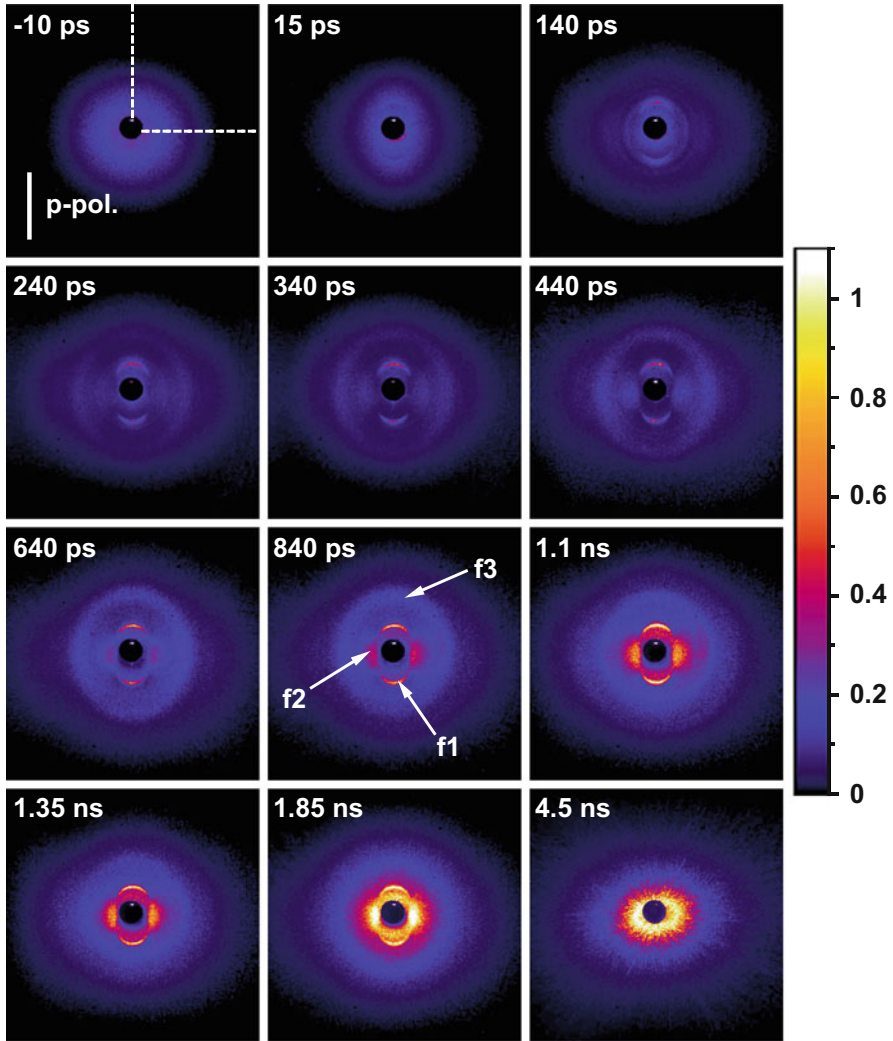
Fig. 6.2 Transient scattering patterns (in false-color representation) of a 100 nm polycrystalline Si-film on a 20 nm Si_3N_4 membrane (size: $100 \times 100\,\mu m^2$) as a function of delay time Δt between the 12 ps, 523 nm optical pump pulse (fluence $\approx$1.7 J/cm^2), and the 10–20 fs, 13.5 nm XUV probe pulse. Displayed spatial frequency range (horizontal and vertical): $-92\,\mu m^{-1}$ to $+92\,\mu m^{-1}$; intensity scale in arbitrary units, but the same for all frames; solid white bar in the first frame: direction of laser polarization (projection onto the surface)

the diameter d of the coherently illuminated sample area can be estimated as $d = 2\pi/\delta q_S \approx 16\,\mu m$, which agrees well with the nominal XUV spot size of $20\,\mu m$ on the sample, highlighting the high spatial coherence of the FEL radiation [39].

The diffraction pattern prior to excitation (-10 ps delay) does reveal that the polycrystalline silicon film has a transverse structure (e.g., grain size) on a hundred nm length scale (as inferred from the width of the measured distribution). Already shortly after excitation, changes of the scattering patterns can be recognized, and three distinct features, in the following denoted as f1, f2, and f3 (marked in the frame for $\Delta t = 840$ ps), develop on different timescales. The most prominent transient feature—f1—is the strong arc-shaped diffraction peaks at $q_v \approx \pm 21 \, \mu m^{-1}$ in the vertical direction. They indicate the formation of a well-oriented structure (perpendicular to the laser polarization) with ≈ 300 nm periodicity. Feature f2 corresponds to the (broader) diffraction peaks at $q_h \approx \pm 15$–$25 \, \mu m^{-1}$ along the horizontal direction (at later times close to the beam stop). Additionally, a broad, ringlike diffraction feature (f3) can be recognized. It has an elliptical shape with (at $\Delta t = 840$ ps) vertical and horizontal half axes of $\approx 43 \, \mu m^{-1}$ and $\approx 36 \, \mu m^{-1}$, corresponding to real space periodicities of ≈ 146 nm and ≈ 175 nm, respectively.

More detailed/quantitative information about the temporal evolution of the different diffraction features is presented in Fig. 6.3. The top row depicts vertical (a) and horizontal (b) cross sections along the white-dashed lines, as shown in the first frame of Fig. 6.2, for selected pump-probe time delays. The bottom row displays time dependencies of (c) the integrated diffraction signal of f1 (red), f2 (blue), and f3 (green), of (d) the (vertical) real space periodicities Λ_{f1} (red) and Λ_{f3} (green) of features f1 and f3, respectively, and of (e) the peak width (FWHM) of f3 (open circles) along the vertical direction and, derived from this width, the effective size of the corresponding *structurally coherent* sample area (filled squares; explanation see below).

Feature f1 starts to form already during the pump laser pulse (2nd frame in Fig. 6.2; green trace $I(q_v)$ in Fig. 6.3a). Its intensity increases with time (red curve in Fig. 6.3c) and it persists until the whole sample starts to disintegrate (last frame in Fig. 6.2, $\Delta t = 4.5$ ns). Moreover, there is a continuous shift in the peak position indicating an increase of its characteristic periodicity Λ_{f1} (red trace in Fig. 6.3d) with time. Feature f2 becomes visible after about 300 ps and its intensity increases subsequently (green trace in Fig. 6.3c). Simultaneously, f2 moves toward smaller q, but an accurate determination of the peak position as a function of delay time is difficult since at early delays, it overlaps with feature f3, while at later delays, it is partially blocked by the beam stop. The elliptical ring feature f3 starts to develop after approximately 100 ps, is most visible after a few hundred ps, and does not persist as long as features f1 and f2. Moreover, its peak position changes with time, being constant for about 400 ps before starting to shift to smaller q_v, which corresponds to an increasing real space periodicity Λ_{f3} (green trace in Fig. 6.3d). Also the width of the ringlike feature f3 changes with time, being constant again for approximately 400 ps followed by a linear decrease, which could be followed until f3 has almost vanished after about 1.4 ns.

All quantities shown in Fig. 6.3c–e for the different features reveal essentially a two-stage evolution of the whole process. During the first stage, up to about 0.4 ns the intensity of f1 and f3 increases, while the intensity of f2 is low. During the same time, Λ_{f1} increases, but Λ_{f3} stays constant. For delay times $\Delta t > 0.4$ ns (stage
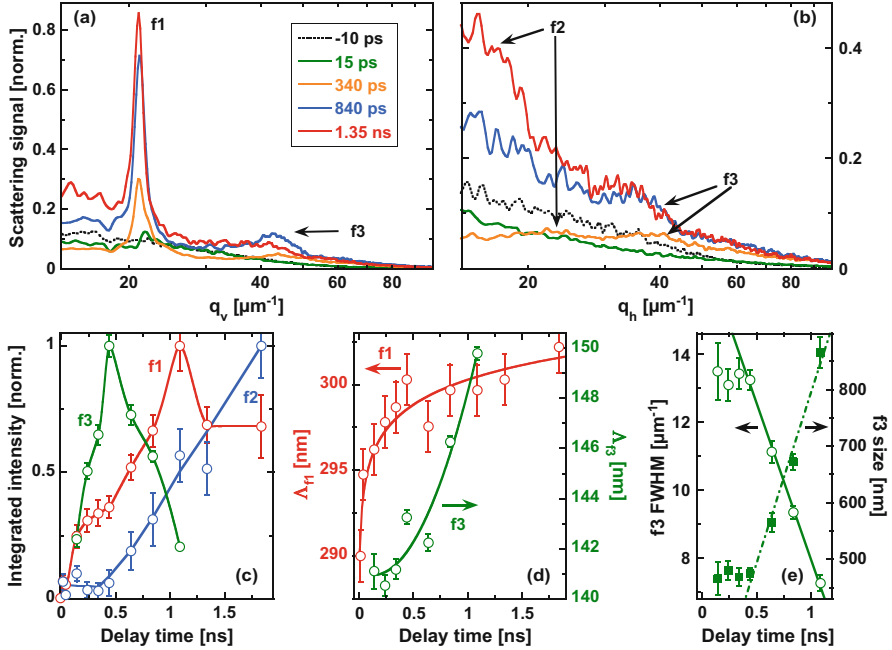
Fig. 6.3 Top row: (**a**) Vertical ($I\,(q_v)$) and (**b**) horizontal ($I\,(q_h)$) cross sections along the white-dashed lines, as shown in the first frame of Fig. 6.2, for selected pump-probe delay times. Bottom row: (**c**) Integrated intensity of the characteristic features f1 (red), f2 (blue), and f3 (green), (**d**) real space periodicities Λ_{f1} of feature f1 (red, left axis) and Λ_{f3} of feature f3 (in vertical direction, green, right axis), (**e**) FWHM of feature f3 (open circles, left axis) and the derived size of the corresponding *structurally coherent* sample area (full squares, right axis), all as a function of pump-probe delay time. The solid curves in (**c**) and (**d**) are a guide to the eye; the curves in (**e**) represent linear fits to the data points at late delay times

2), f1 exhibits a further increase in intensity, which levels off around 1 ns, while the intensity of f2 starts to continuously increase, and f3 decreases in intensity. Similarly, while Λ_{f1} remains essentially constant, Λ_{f3} increases and the f3 peak width decreases.

4 Discussion and Interpretation of the Transient Scattering Patterns

Before discussing and interpreting the experimental results, we would like to point out that *any* spatially dependent modulation of the optical properties (in the XUV!) of the laser-excited material will result in scattering of the probe beam. Such modulation can be caused by a variety of processes, such as electronic excitation, ionization, heating, but also changes in density and surface topography due to

material expansion and ablation. Therefore, it is a priori difficult if not impossible to disentangle these processes from the scattering data without further knowledge, for example, through their characteristic timescales. Most likely, the scattering observed at early delay times has to be attributed to electronic excitation and melting of the material, whereas at later times, density modulations and changes of the surface topography due to expansion and ablation dominate.

To interpret the experimental data and the different diffraction features, we apply first the intuitive model of interference between the incident laser field and surface scattered/excited waves since it allows simple predictions on the periodicity and angular orientation of the resulting LIPSS. This is illustrated in Fig. 6.4 where $\mathbf{k}_p$ denotes the in-surface component of the wave-vector $\mathbf{k}_i$ of the incident pump laser beam ($k_p = k_i \cdot \sin(\alpha)$; α: angle of incidence) and $\mathbf{k}_s$ the wave-vector of a scattered/excited wave propagating along the surface.

While $\mathbf{k}_s$ can have, in principle, any in-plane direction, its length is determined by the particular nature of the scattering/excitation process. Often it has been found that $k_s \approx k_i$ and the LIPSS wave-vector $\mathbf{q}_l$ is then given by $\mathbf{q}_l = \pm(\mathbf{k}_p + \mathbf{k}_s)$. Therefore, all possible $\mathbf{q}_l$ lie on two intersecting circles with radius $k_p \approx k_i$ centered at $\pm\mathbf{k}_p$. Moreover, in many experiments (e.g., [40]), three dominating LIPSS modes were found for p-polarized light. The first two modes $q_l^{\pm}$ correspond to $\mathbf{k}_s$ parallel or antiparallel to $\mathbf{k}_p$, and the third mode q_l^0 to the intersection points of the two circles. For these cases, $q_l^{\pm} = (k_i \pm k_p) = k_i \cdot (1 \pm \sin(\alpha))$ and $q_l^0 = k_i \cdot \cos(\alpha)$, which results in $q_l^+ = 20.8\,\mu m^{-1}$, $q_l^- = 3.2\,\mu m^{-1}$, and $q_l^0 = 8.1\,\mu m^{-1}$ here. The corresponding LIPSS periodicities $\Lambda_l = 2\pi/q_l$ are $\Lambda_l^+ = 302\,nm$, $\Lambda_l^- = 1.95\,\mu m$, and $\Lambda_l^0 = 780\,nm$. While q_l^- and q_l^0 are blocked by the beam stop, it seems natural to identify the arc-shaped diffraction feature f1 as segments of the intersecting
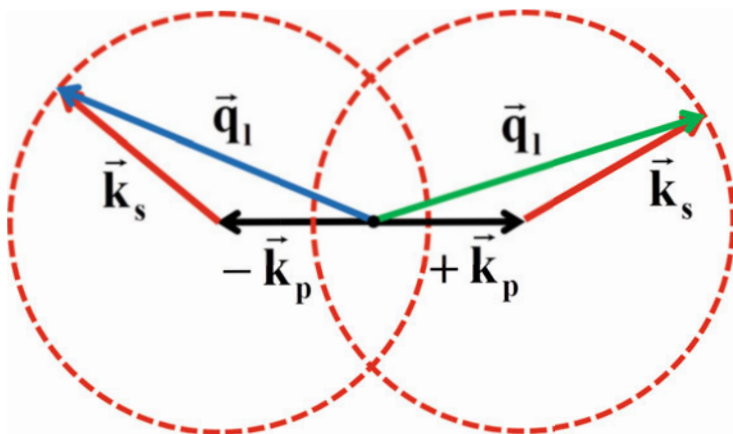

Fig. 6.4 Interference model for LIPSS generation: $\mathbf{k}_p$, in-surface component of the wave-vector $\mathbf{k}_i$ of the incident pump laser beam with $k_p = k_i \cdot \sin(\alpha)$; $\mathbf{k}_s$, wave-vector of a scattered/excited wave propagating along the surface; $\mathbf{q}_l$, LIPSS wave-vector
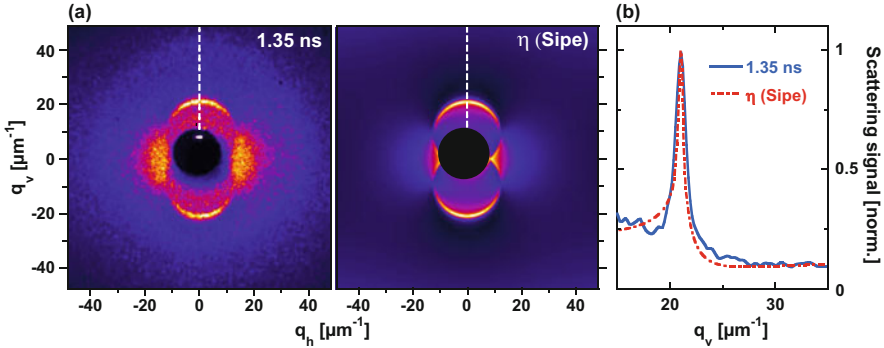
Fig. 6.5 (**a**) Comparison of the transient scattering pattern measured at $\Delta t = 1.35$ ns and calculations of the so-called efficacy factor η based on the model by Sipe et al. [5]. (**b**) Vertical cross sections (normalized) in the vicinity of the q_l^+-peak (red, η (q_v); blue, I (q_v, 1.35 ns)

circles and the f1-peak in the circles and the f1-peak in the I (q_v)-profiles (Fig. 6.3a) as the q_l^+ LIPSS mode.

Going beyond the simplified interference model, the theory of Sipe et al. is applied [5, 41]. It allows to calculate the so-called efficacy factor $\eta(\mathbf{q})$, which is proportional to the spatially varying deposition of the laser pulse energy (represented in Fourier space). Among other factors, it depends on the optical constants of the irradiated material (for further details, the reader is referred to [41, 42]). Figure 6.5a compares the transient scattering pattern measured at $\Delta t = 1.35$ ns to a calculated distribution of η for the parameters of our experiment (i.e., laser wavelength, polarization, and angle of incidence) using the optical constants of liquid Si as input.

The agreement between the calculated efficacy factor and the measured scattering pattern is striking and almost quantitative (at least in certain q-ranges) as indicated by the vertical cross sections around the q_l^+-peak shown in Fig. 6.5b. This unambiguously confirms the assignment of f1 made above. In the classification of the recent LIPSS literature [17], f1 is associated with type-s LSFL. It should be noted that the good agreement between the calculated η and the measured experimental diffraction pattern is achieved only when using the optical constants of liquid Si (which is metallic) as input. Given the high pump fluence well above the melting and ablation threshold, this appears not surprising because melting will occur already during the 12 ps duration laser pulse.

However, the efficacy factor η (**q**) does not provide information on how and on which timescales such a modulated energy deposition transforms into modifications of the sample properties and morphology responsible for the transient scattering measured in the experiment. Moreover, the Sipe model, as applied here, does not take into account changes of the sample (morphology, optical properties) during irradiation, which are very likely to occur for the conditions of our experiment (12 ps pulse duration, high fluence) when the material transforms already during the pulse

from a cold solid, over a hot, electronically excited semiconductor into a metallic liquid. Such changes will definitely influence the process of LIPSS formation (e.g., Bonse et al. [42] have argued for the case of fs laser-excited Si that changes of the optical properties caused by the formation of a dense electron-hole plasma can change the LIPSS periodicity).

However, we believe that the increase of the real space periodicity Λ_{f1} of the f1 feature (Fig. 6.3d) observed here is only an apparent one since this would imply a corresponding expansion of the LIPSS pattern over the whole pump laser spot size of 40 μm in horizontal direction, requiring lateral expansion velocities initially in excess of 5 km/s, which appears unrealistic.

Pfau et al. [43] have observed changes of positions of diffraction peaks of similar magnitude (i.e., a few percent) in time-resolved magnetic scattering experiments (performed also at FLASH) during the ultrafast, laser-induced demagnetization of a thin-film Co/Pt multilayer. These samples exhibit a pronounced "wormlike" structure of domains with opposite magnetization, which gives rise to a characteristic diffraction ring. The peak position of this diffraction ring shifts to lower q within a few hundred femtoseconds after laser excitation, which is attributed to changes of the scattering form factor due to a smoothing of the magnetization profile at the domain boundary caused by spin-dependent carrier transport.

We think a similar form factor effect is responsible for the observed shift of the f1 peak—although on a very different timescale. The spatially periodic energy deposition (as described by the efficacy factor) transfers—very likely in a nonlinear fashion—into a corresponding modulation of the material properties (e.g., temperature, melt depth), thus imposing lateral gradients of these properties. These will smooth out with time due to lateral transport (e.g., heat conduction), which may affect the form factor in a similar way as discussed in [43].

Considering only Fig. 6.5, it is tempting to interpret f2 also with the help of the Sipe model and the efficacy factor as the "tail" of scattering signal originating from the vicinity of q_l^0/q_l^-. We exclude this explanation because the f2 feature appears significantly later than f1 and is initially well separated from the beam stop (see the orange $I(q_h)$-trace in Fig. 6.3) and thus q_l^0. However, the limited signal-to-noise ratio of the data in the q-range of the f2 feature does not allow for further quantitative analysis, so we refrain from speculating on its physical origin at this point.

Similarly, the calculated η does not account for the elliptical f3 feature, which is strongest for $\Delta t < 1$ ns and which has almost vanished at $\Delta t = 1.35$ ns. As a possible origin of the f3 feature, we suggest the formation of capillary waves at the surface of the laser-molten silicon film [19, 21], presumably excited through the recoil of ablating material. This scenario is supported by the timescales of the appearance of this feature at delay times $\Delta t \approx 100$ ps [44]. For a quantitative analysis, we neglect gravitational forces (i.e., large capillary constant $a = \sqrt{\frac{2\sigma}{g\rho}}$ [45]; g gravitational acceleration, σ surface tension, ρ density) and apply the dispersion relation of capillary waves in the short wavelength limit (eq. 62.3 in [45]). This results in an oscillation period $T = \sqrt{\frac{\Lambda^3 \rho}{2\pi\sigma}}$ (Λ wavelength of the capillary waves).

Identifying Λ with $\Lambda_{f3} \approx 140\,\text{nm}$ at early delay times (stage 1) and using published values for the density $\rho = 2.52\,\text{g/cm}^3$ and the surface tension $\sigma = 0.874$ kg/s^2 of liquid silicon at the melting point [46], we obtain a half oscillation period of $T/2 \lesssim 0.6\,\text{ns}$, in reasonable agreement with the temporal evolution (rise and subsequent decay) of the intensity of the f3 feature [19]. Within this picture, f3 does not reappear since these short wavelength capillary waves are damped by viscous forces with a damping time $\tau_D = \frac{\rho \Lambda^2}{8\pi^2 \eta} \approx 2.8\,\text{ns}$ ($\eta \approx 0.8\,\text{mPa·s}$: dynamic viscosity of liquid silicon [47]) and additionally laser-induced ablation decomposes the molten silicon film on the ns timescale. With respect to the observed time-dependent increase of Λ_{f3}, similar form factor changes might be responsible as discussed above for the LIPSS periodicity Λ_{f1}.

Finally, we interpret the peak width w (FWHM) of the f3 feature, as depicted by the open circles in Fig. 6.3e, in a Scherrer-like approach [48] as a measure of the size $s \approx 2\pi/w$ of the area, where capillary waves are *coherently* excited. This size (filled squares in Fig. 6.3e) has an approximately constant value of 470 nm during stage 1, but increases linearly with a slope of $v = 600\,\text{m/s}$ (dashed-dotted curve in Fig. 6.3e) during stage 2. Within the capillary wave picture, v corresponds to twice the group velocity v_G of the excited waves assuming that the initial excitation area expands radially by capillary wave propagation. However, one must take into account that the value of a (and thus v) derived from the f3 peak width w with the equation above tends to overestimate the actual size for two reasons [49]: (i) The Scherrer equation includes a pre-factor K, which depends on the shape of the scattering object and is usually somewhat smaller than 1; (ii) the determined value of a represents in our case (2D scattering objects) an area-weighted mean value, which depends on the size distribution (unknown), but emphasizes larger *particles*. Therefore, $v/2 = 300\,\text{m/s}$ represents actually an upper boundary for the group velocity v_G of capillary waves, which can be theoretically calculated from the dispersion relation as $v_G = d\omega/dk = \frac{3}{2} \cdot \sqrt{\frac{2\pi\sigma}{\rho\Lambda}}$. Using again the published values for density ρ and surface tension σ of liquid silicon [46], we obtain $v_G \approx 180\,\text{m/s}$, in reasonable agreement with the upper boundary $v/2 = 300\,\text{m/s}$ determined from the observed decrease of the f3 peak width.

In summary, although we ignore any temperature-dependent changes of the thermophysical material properties, the simple capillary wave picture provides a surprisingly good quantitative description of the temporal evolution of the f3 feature. However, two questions remain unanswered: (i) What mechanism selects the observed wavelength Λ_{f3} and (ii) why is the f3 diffraction ring elliptical? As we will argue in the next section, both effects may be related to the f1 feature and the formation of type-s LSFL.

5   Polarization Dependence

The Sipe model allows predictions how the LIPSS formation depends on laser polarization [5, 40]. In particular, it is expected (and has been experimentally confirmed) that upon rotation of the pump laser polarization, the arc segments, where $\eta\,(\mathbf{q})$ is maximum, rotate as well. To validate this, the XUV scattering on a similar 100-nm-thick Si film for similar[2] excitation conditions as above has been measured for three different polarization directions (p-, s-, and 45°-polarization). Data for a pump-probe delay of $\Delta t = 340$ ps are shown in Fig. 6.6.

It has to be noted that these measurements have been performed with silicon films deposited on smaller, $20 \times 20\,\mu m^2$-sized Si_3N_4 membranes. Diffraction from the edges of the membranes is responsible for the very intense vertical and horizontal streaks (white), which partially overlap with the different scattering features discussed above. However, in complete agreement with the Sipe model, the f1 feature moves along the two intersecting circles depicted in Fig. 6.4 and is weakest for s-polarized pump light. Although the f2 feature is not visible for s-polarized excitation, presumably because the scattering intensity is low (as for f1) and superimposed by the strong scattering from the membrane edges, Fig. 6.6 clearly demonstrates that the diffraction features f2 and f3 change their orientation as well. However, while the motion of f1 is centered around $\pm\mathbf{k}_p$, f2 and f3 rotate around the origin $\mathbf{q} = 0$. As such, the elliptical f3 feature keeps its large axis always
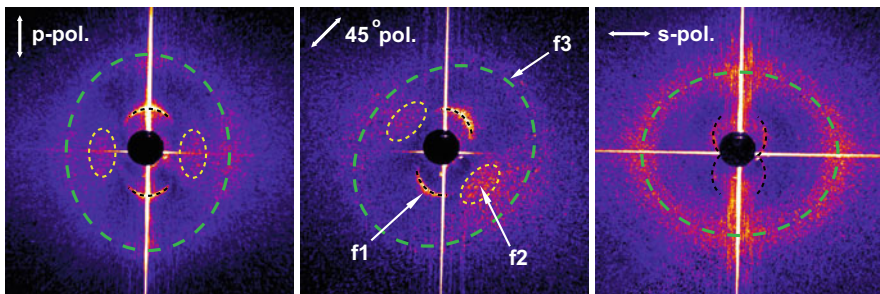

Fig. 6.6 Transient scattering patterns of a 100 nm polycrystalline Si film (on a $20 \times 20\,\mu m^2$, 20-nm-thick Si_3N_4 membrane) measured 340 ps after excitation with a 12 ps, 523 nm laser pulse (fluence ≈ 2 J/cm^2) for different polarization directions (left, p-pol.; middle, 45°-pol.; right, s-pol.). The black, yellow, and green dashed curves mark the characteristic diffraction features f1, f2, and f3, respectively. Please note that the intensity scale has been adjusted for each image separately in order to make the different diffraction features clearly visible. The overall scattering intensity is decreasing by changing the pump polarization from p to s

---

[2] For the measurements with 45°- and s-polarized pumping, we increased the laser fluence to the maximum available level of about 2.2 J/cm^2 to account at least partly for the increased reflection losses compared to pumping with p-polarized light.

parallel to the linear laser beam polarization (the aspect ratio does not change), while the f2 feature is always oriented perpendicular to it.

To explain this behavior, one has to consider that the modulated energy deposition at the spatial frequency q_l^+ of the f1 feature, which leads to LIPSS formation, also imposes an overall asymmetry of the transient material properties and consequently in the material dynamics between directions along and perpendicular to the pump laser polarization. Since the f1 feature appears first (already during the pulses), it may be not surprising that the processes leading to the f2 and f3 diffraction features depend on the pump pulse polarization in the observed manner (rotation with the polarization, ellipticity of f3), although f2 and f3 are not accounted for by the efficacy factor η (**q**). In fact, in Chap. 5 of this book, Rudenko and Colombier discuss various mechanisms (e.g., near-field effects) that lead to a polarization-dependent symmetry breaking and thus preferred orientation of the evolving structures. In addition, it is noteworthy that $\Lambda_{f3} \approx \Lambda_{f1}/2$, which points toward a further connection between the f1 and f3 features, suggesting that the so far not understood selection of wavelength within the capillary wave picture is also related to the periodically modulated energy deposition.

6 Higher-Order LIPSS

In this section, we discuss results from a scattering experiment in a similar experimental geometry, but using single 50 fs, 800 nm, and p-polarized laser pulses at an angle of incidence of 45° (p-pol.) for the excitation of approximately $5 \times 5\,\mu m^2$ sized Si patches of 100 nm thickness deposited on free-standing 20-nm-thick Si_3N_4 membranes (see inset in the upper-left frame in Fig. 6.7) at a fluence again well above the ablation threshold. For several reasons not be discussed here, we were not able to perform systematic measurements, but only to record a limited number of scattering patterns. A short sequence of those are shown in Fig. 6.7 for different pump-probe time delays. As in Fig. 6.2, the projection of the pump laser beam polarization (p-pol.) onto the sample surface is indicated by the vertical solid white bar in the first frame of Fig. 6.7.

Please note that in order to make diffraction features at larger scattering angles visible (e.g., scattering pattern at $\Delta t = 0.4$ ns), high FEL intensities were required leading to saturation of the detector closer to the beam stop. The saturated region was smeared out further in vertical direction due to the read-out process of the CCD detector.

The upper-left pattern measured at negative time delay shows the scattering of the unperturbed Si patch. Two features of the scattering patterns measured at positive delay times are particularly noteworthy:

(1) The f1 feature, which is characteristic for type-s LSFL as predicted by the Sipe model, is observed even after excitation with a single fs pulse. Since the pump spot size on the sample is larger than the actual sample size, we
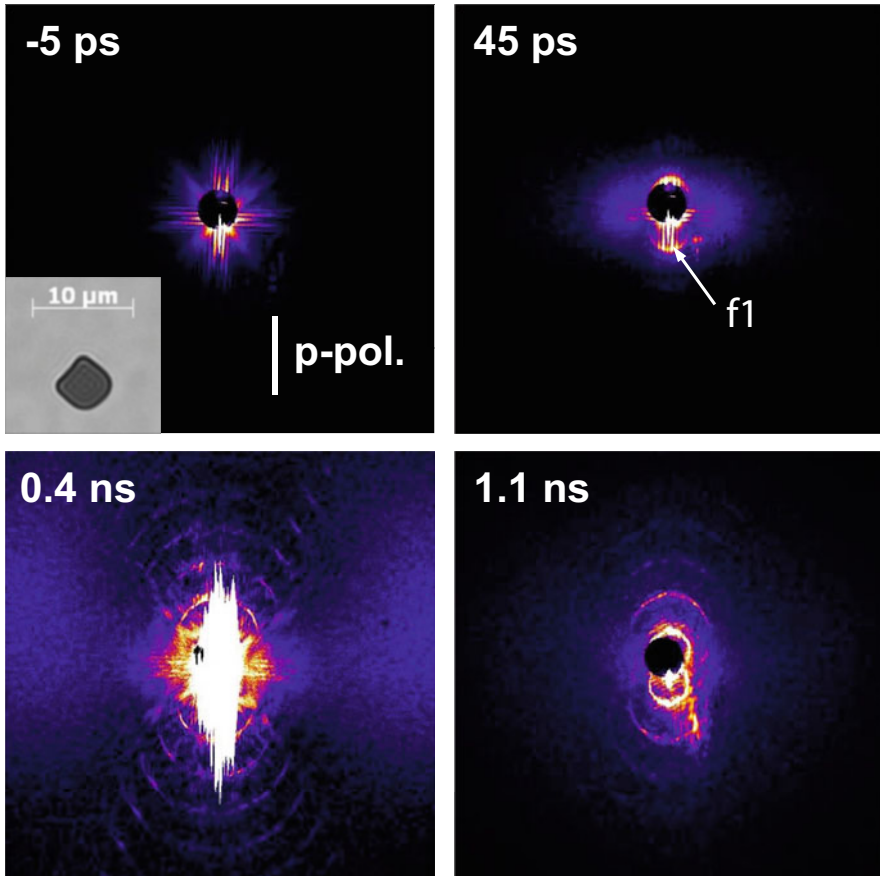
Fig. 6.7 Transient scattering pattern of $5 \times 5\,\mu m^2$ sized Si patches of 100 nm thickness deposited on free-standing 20-nm-thick Si_3N_4 membranes after excitation with a 50 fs, 800 nm laser pulse for different pump-probe delay times; solid white bar in the first frame: direction of laser polarization (projection onto the surface). The inset in the upper-left frame shows an optical micrograph of a typical sample

attribute this to efficient scattering of the pump radiation at the edges of the Si patch, similar to the observations on surfaces, which have been intentionally pre-structured/scratched [26, 29].

(2) As is best visible in the two scattering patterns at larger delays, not only the fundamental of the f1 feature is observed but also higher diffraction orders (we were able to detect scattering up to the 9th order) indicating that the spatial modulation of the material properties that give rise to the scattering of the XUV probe pulse is non-sinusoidal. These higher orders are observed at longer delay times and can be, therefore, very likely associated with changes of the sample morphology due to a spatially modulated ablation of the material. Since ablation

exhibits generally a nonlinear dependence on fluence (e.g., threshold behavior), a non-sinusoidal surface morphology will develop even for a sinusoidally modulated energy deposition leading to higher-order diffraction.

We would like to emphasize that these results, although not yet systematic, specifically highlight the advantage of probing the LIPSS dynamics with short wavelength radiation. Higher-order transient diffraction from LIPSS has so far been reported only in the work by Keilmann [19], who observed second-order LIPSS diffraction after excitation with a CO_2 laser (wavelength $10.6\,\mu m$). In all other studies, the accessible momentum transfer range was not sufficient to capture these details.

7 Summary and Outlook

The formation of LIPSS (and structure formation in general) at laser-irradiated surfaces represents a complex multiscale problem in terms of the relevant length and timescales, as well as the underlying physical processes, posing extreme challenges for their experimental and theoretical investigation.

On the experimental side, techniques are required that combine high temporal resolution down to the femtosecond range with the appropriate spatial resolution on the nanometer to micrometer scale. Furthermore, these techniques need to be applied under highly irreversible conditions where single pulse laser excitation leads to significant permanent changes of the irradiated surface area.

In this contribution, we have presented a set of time-resolved scattering experiments using femtosecond XUV pulses from a FEL that allowed us to follow directly structure formation at the surface of thin silicon films after irradiation with picosecond optical laser pulses on sub-micrometer to nanometer length scales.

Although the measured data reveal a complex evolution both, in time and momentum space, the main aspects are accounted for by the LIPSS model of Sipe et al. [5], which is confirmed almost quantitatively. However, the additional diffraction features observed here and their complex temporal evolution reveal the relevance of other processes (e.g., excitation of capillary waves).

Due to time constraints—the presented data represent results from approx. 48 h of FEL beamtime—more detailed and systematic studies had not been possible. Nevertheless, our experiments represent the first step towards more thorough investigations of nanoscale structure formation (incl. LIPSS) at laser-irradiated surface on extreme time and length scales that have not been accessible before.

While the extension of these experiments toward shorter probing wavelengths will enable measurements with even higher spatial resolution, the application of a grazing-incidence scattering geometry [50] will allow to study the surfaces of bulk materials, a situation more typical/relevant in *real-life* laser processing. Similarly, the technique can be also applied in the multi-pulse excitation regime by pre-structuring the surface through irradiation with N laser pulses and probing the

transient changes induced by the $(N + 1)$ excitation pulse, as has been done in all-optical pump-probe experiments (e.g., [23, 25]). On the other hand, 3D tomography using multiple probe pulses at different angles of incidence may provide volumetric information.

Moreover, experimental schemes that make use of the very high spatial coherence of the FEL radiation, like coherent diffraction imaging [37] and photon correlation spectroscopy (e.g., [51, 52]), can provide additional opportunities. In fact, during the same beamtime, where the data presented here have been measured, we have additionally used both techniques to follow in real space with nanometer resolution and on picosecond timescales the laser-induced destruction of a fabricated nanostructure [35].

With respect to the theoretical description of these processes, such experiments, in particular if scattering intensities can be properly calibrated/normalized, should provide important benchmark data for the sophisticated hybrid electromagnetic and hydrodynamic continuum models (see, e.g., [14] and Chap. 5 of this book) that have been developed recently.

References

1. B. Rethfeld, K. Sokolowski-Tinten, D. von der Linde, S.I. Anisimov, Appl. Phys. A: Mater. Sci. Process. **79**, 767 (2004). https://doi.org/10.1007/s00339-004-2805-9
2. M. Birnbaum, J. Appl. Phys. **36**(11), 3688 (1965). https://doi.org/10.1063/1.1703071
3. C. Florian, S.V. Kirner, J. Krüger, J. Bonse, J. Laser. Appl. **32**(2), 022063 (2020). https://doi.org/10.2351/7.0000103
4. D.C. Emmony, R.P. Howson, L. J. Willis, Appl. Phys. Lett. **23**(11), 598 (1973). https://doi.org/10.1063/1.1654761

5. J.E. Sipe, J.F. Young, J.S. Preston, H.M. van Driel, Phys. Rev. B **27**, 1141 (1983). https://doi.org/10.1103/PhysRevB.27.1141
6. D. Dufft, A. Rosenfeld, S.K. Das, R. Grunwald, J. Bonse, J. Appl. Phys. **105**(3), 034908 (2009). https://doi.org/10.1063/1.3074106
7. J.Z.P. Skolski, G.R.B.E. Römer, J.V. Obona, V. Ocelik, A.J. Huis in 't Veld, J.T.M. De Hosson, Phys. Rev. B **85**, 075320 (2012). https://doi.org/10.1103/PhysRevB.85.075320
8. S. Höhm, A. Rosenfeld, J. Krüger, J. Bonse, J. Appl. Phys. **112**, 014901 (2012). https://doi.org/10.1063/1.4730902
9. A. Rudenko, J.P. Colombier, S. Höhm, A. Rosenfeld, J. Krüger, J. Bonse, T.E. Itina, Sci. Rep. **7**, 12306 (2017). https://doi.org/10.1038/s41598-017-12502-4
10. T.Q. Jia, H.X. Chen, M. Huang, F.L. Zhao, J.R. Qiu, R.X. Li, Z.Z. Xu, X.K. He, J. Zhang, H. Kuroda, Phys. Rev. B **72**, 125429 (2005). https://doi.org/10.1103/PhysRevB.72.125429
11. X. Guo, R. Li, Y. Hang, Z. Xu, B. Yu, H. Ma, B. Lu, X. Sun, Mater. Lett. **62**, 1769 (2008). https://doi.org/10.1016/j.matlet.2007.09.082
12. F. Costache, S. Kouteva-Arguirova, J. Reif, Appl. Phys. A: Mater. Sci. Process. **79**, 1429 (2004). https://doi.org/10.1007/s00339-004-2803-y
13. J. Reif, O. Varlamova, F. Costache, Appl. Phys. A: Mater. Sci. Process. **92**, 1019 (2008). https://doi.org/10.1007/s00339-008-4671-3
14. A. Rudenko, A. Abou-Saleh, F. Pigeon, C. Mauclair, F. Garrelie, R. Stoian, J.P. Colombier, Acta Mater. **194**, 93 (2020). https://doi.org/10.1016/j.actamat.2020.04.058
15. J. Bonse, S. Höhm, S.V. Kirner, A. Rosenfeld, J. Krüger, IEEE J. Sel. Top. Quantum Electron. **23**, 9000615 (2017). https://doi.org/10.1109/JSTQE.2016.2614183
16. J. Bonse, Nanomaterials **10**, 1950 (2020). https://doi.org/10.3390/nano10101950
17. J. Bonse, S. Gräf, Laser Photon. Rev. **14**, 2000215 (2020). https://doi.org/10.1002/lpor.202000215
18. D.J. Ehrlich, S.R.J. Brueck, J.Y. Tsao, Appl. Phys. Lett. **41**, 630 (1982). https://doi.org/10.1063/1.93631
19. F. Keilmann, Phys. Rev. Lett. **51**, 2097 (1983). https://doi.org/10.1103/PhysRevLett.51.2097
20. J.F. Young, J.S. Preston, J.E. Sipe, H.M. van Driel, Phys. Rev. B **27**, 1424 (1983). https://doi.org/10.1103/PhysRevB.27.1424
21. J.F. Young, J.E. Sipe, H.M. van Driel, Phys. Rev. B **30**, 2001 (1984). https://doi.org/10.1103/PhysRevB.30.2001
22. T.D. Lee, H.W. Lee, C.H. Nam, J.K. Kim, C.O. Park, J. Appl. Phys. **71**, 4208 (1992). https://doi.org/10.1063/1.350799
23. S. Höhm, A. Rosenfeld, J. Krüger, J. Bonse, Appl. Phys. Lett. **102**, 054102 (2013). https://doi.org/10.1063/1.4790284
24. R.D. Murphy, B. Torralva, D.P. Adams, S.M. Yalisove, Appl. Phys. Lett. **103**, 141104 (2013). https://doi.org/10.1063/1.4823588
25. X. Jia, T.Q. Jia, N.N. Peng, D.H. Feng, S.A. Zhang, Z.R. Sun, J. Appl. Phys. **115**, 143102 (2014). https://doi.org/10.1063/1.4870445
26. K.R.P. Kafka, D.R. Austin, H. Li, A.Y. Yi, J. Cheng, E.A. Chowdhury, Opt. Express **23**, 19432 (2015). https://doi.org/10.1364/OE.23.019432
27. M. Garcia-Lechuga, D. Puerto, Y. Fuentes-Edfuf, J. Solis, J. Siegel, ACS Photon. **3**, 1961 (2016). https://doi.org/10.1021/acsphotonics.6b00514
28. K. Zhou, X. Jia, T. Jia, K. Cheng, K. Cao, S. Zhang, D. Feng, Z. Sun, J. Appl. Phys. **121**, 104301 (2017). https://doi.org/10.1063/1.4978375
29. J. Liu, X. Jia, W. Wu, K. Cheng, D. Feng, S. Zhang, Z. Sun, T. Jia, Opt. Express **26**, 6302 (2018). https://doi.org/10.1364/OE.26.006302
30. V. Ayvazyan, N. Baboi, J. Bähr, V. Balandin, B. Beutner, A. Brandt, I. Bohnet, A. Bolzmann, R. Brinkmann, O. Brovko, J. Carneiro, S. Casalbuoni, M. Castellano, P. Castro, L. Catani, E. Chiadroni, S. Choroba, A. Cianchi, H. Delsim-Hashemi, G.D. Pirro, M. Dohlus, S. Düsterer, H. Edwards, B. Faatz, A. Fateev, J. Feldhaus, K. Flöttmann, J. Frisch, L. Fröhlich, T. Garvey, U. Gensch, N. Golubeva, H.J. Grabosch, B. Grigoryan, O. Grimm, U. Hahn, J. Han, M. v. Hartrott, K. Honkavaara, M. Hüning, R. Ischebeck, E. Jaeschke, M. Jablonka, R. Kam-

mering, V. Katalev, B.K.S. Khodyachykh, Y. Kim, V. Kocharyan, M. Körfer, M. Kollewe, D. Kostin, D. Krämer, M. Krassilnikov, G. Kube, L. Lilje, T. Limberg, D. Lipka, F. Löhl, M. Luong, C. Magne, J. Menzel, P. Michelato, V. Miltchev, M. Minty, W. Möller, L. Monaco, W. Müller, M. Nagl, O. Napoly, P. Nicolosi, D. Nölle, T.N. nez, A. Oppelt, C. Pagani, R. Paparella, B. Petersen, B. Petrosyan, J. Pflüger, P. Piot, E. Plönjes, L. Poletto, D. Proch, D. Pugachov, K. Rehlich, D. Richter, S. Riemann, M. Ross, J. Rossbach, M. Sachwitz, E.L.Saldin, W. Sandner, H. Schlarb, B. Schmidt, M. Schmitz, P. Schmüser, J. Schneider, E. Schneidmiller, H.J. Schreiber, S. Schreiber, A. Shabunov, D. Sertore, S. Setzer, S. Simrock, E. Sombrowski, L. Staykov, B. Steffen, F. Stephan, F. Stulle, K. Sytchev, H. Thom, K. Tiedtke, M. Tischer, R. Treusch, D. Trines, I. Tsakov, A. Vardanyan, R. Wanzenberg, T. Weiland, H. Weise, M. Wendt, I. Will, A. Winter, K. Wittenburg, M. Yurkov, I. Zagorodnov, P. Zambolin, K. Zapfe, Eur. Phys. J. D **37**, 297 (2006). https://doi.org/10.1140/epjd/e2005-00308-1

31. K. Sokolowski-Tinten, A. Barty, S. Boutet, U. Shymanovich, H. Chapman, M. Bogan, S. Marchesini, S. Hau-Riege, N. Stojanovic, J. Bonse, Y. Rosandi, H.M. Urbassek, R. Tobey, H. Ehrke, A. Cavalleri, S. Düsterer, H. Redlin, M. Frank, S. Bajt, J. Schulz, M. Seibert, J. Hajdu, R. Treusch, C. Bostedt, M. Hoener, T. Möller, AIP Conf. Proc. **1278**, 373 (2010). https://doi.org/10.1063/1.3507123

32. C. Bostedt, H.N. Chapman, J.T. Costello, J.R. Crespo López-Urrutia, S. Düsterer, S.W. Epp, J. Feldhaus, A. Föhlisch, M. Meyer, T. Möller, R. Moshammer, M. Richter, K. Sokolowski-Tinten, A. Sorokin, K. Tiedtke, J. Ullrich, W. Wurth, Nucl. Instrum. Methods Phys. Res. A **601**, 108 (2009). http://doi.org/10.1016/j.nima.2008.12.202. Special issue in honour of Prof. Kai Siegbahn

33. J. Rossbach, J.R. Schneider, W. Wurth, Phys. Rep. **808**, 1 (2019). https://doi.org/10.1016/j.physrep.2019.02.002

34. K. Tiedtke, A. Azima, N. von Bargen, L. Bittner, S. Bonfigt, S. Düsterer, B. Faatz, U. Frühling, M. Gensch, C. Gerth, N. Guerassimova, U. Hahn, T. Hans, M. Hesse, K. Honkavaar, U. Jastrow, P. Juranic, S. Kapitzki, B. Keitel, T. Kracht, M. Kuhlmann, W.B. Li, M. Martins, T. Núñez, E. Plönjes, H. Redlin, E.L. Saldin, E.A. Schneidmiller, J.R. Schneider, S. Schreiber, N. Stojanovic, F. Tavella, S. Toleikis, R. Treusch, H. Weigelt, M. Wellhöfer, H. Wabnitz, M.V. Yurkov, J. Feldhaus, New J. Phys. **11**, 023029 (2009). https://doi.org/10.1088/1367-2630/11/2/023029

35. A. Barty, S. Boutet, M.J. Bogan, S. Marchesini, K. Sokolowski-Tinten, N. Stojanovic, R. Tobey, H. Ehrke, A. Cavalleri, S. Düsterer, M. Frank, S. Bajt, B.W. Woods, M.M. Seibert, J. Hajdu, R. Treusch, H.N. Chapman, Nat. Photon. **2**, 415 (2008). https://doi.org/10.1038/nphoton.2008.128

36. S. Bajt, H.N. Chapman, E.A. Spiller, J.B. Alameda, B.W. Woods, M. Frank, M.J. Bogan, A. Barty, S. Boutet, S. Marchesini, S.P. Hau-Riege, J. Hajdu, D. Shapiro, Appl. Opt. **47**, 1673 (2008). https://doi.org/10.1364/AO.47.001673

37. H.N. Chapman, A. Barty, M.J. Bogan, S. Boutet, M. Frank, S.P. Hau-Riege, S. Marchesini, B.W. Woods, S. Bajt, W.H. Benner, R.A. London, E. Plönjes, M. Kuhlmann, R. Treusch, S. Düsterer, T. Tschentscher, J.R. Schneider, E. Spiller, T. Möller, C. Bostedt, M. Hoener, D.A. Shapiro, K.O. Hodgson, D. van der Spoel, F. Burmeister, M. Bergh, C. Caleman, G. Huldt, M.M. Seibert, F.R. Maia, R.W. Lee, A. Szoke, N. Timneanu, J. Hajdu, Nat. Phys. **2**, 839 (2006). https://doi.org/10.1038/nphys461

38. H. Redlin, A. Al-Shemmary, A. Azima, N. Stojanovic, F. Tavella, I. Will, S. Düsterer, Nucl. Instr. Meth. Phys. Res. A **635**, S88 (2011). https://doi.org/10.1016/j.nima.2010.09.159

39. A. Singer, I.A. Vartanyants, M. Kuhlmann, S. Duesterer, R. Treusch, J. Feldhaus, Phys. Rev. Lett. **101**, 254801 (2008). https://doi.org/10.1103/PhysRevLett.101.254801

40. J.F. Young, J.S. Preston, H.M. van Driel, J.E. Sipe, Phys. Rev. B **27**, 1155 (1983). https://doi.org/10.1103/PhysRevB.27.1155

41. J. Bonse, M. Munz, H. Sturm, J. Appl. Phys. **97**, 013538 (2005). https://doi.org/10.1063/1.1827919

42. J. Bonse, A. Rosenfeld, J. Krüger, J. Appl. Phys. **106**, 104910 (2009). https://doi.org/10.1063/1.3261734

43. B. Pfau, S. Schaffert, L. Müller, C. Gutt, A. Al-Shemmary, F. Büttner, R. Delaunay, S. Düsterer, S. Flewett, R. Frömter, J. Geilhufe, E. Guehrs, C.M. Günther, R. Hawaldar, M. Hille, N. Jaouen, A. Kobs, K. Li, J. Mohanty, H. Redlin, W.F. Schlotter, D. Stickler, R. Treusch, B. Vodungbo, M. Kläui, H.P. Oepen, J. Lüning, G. Grübel, S. Eisebitt, Nat. Commun. **3**, 1100 (2012). https://doi.org/10.1038/ncomms2108

44. K. Sokolowski-Tinten, J. Bialkowski, A. Cavalleri, D. von der Linde, Appl. Surf. Sci. **127-129**, 755 (1998). https://doi.org/10.1016/S0169-4332(97)00736-8

45. L.D. Landau, E.M. Lifshitz, *Fluid Mechanics*. Course of Theoretical Physics, vol. 6, 2nd edn. (Pergamon, 1987)

46. S. Nakamura, T. Hibiya, Int. J. Thermophys. **13**, 1061 (1992). https://doi.org/10.1007/BF01141216

47. K.W. Kolasinski, Curr. Opin. Solid State Mater. Sci. **11**, 76 (2007). https://doi.org/10.1016/j.cossms.2008.06.004

48. P. Scherrer, Nachrichten Gesellschaft der Wissenschaften zu Göttingen (Mathematisch-Physikalische Klasse, 1918), pp. 98–100

49. J.I. Langford, A.J.C. Wilson, J. Appl. Crystallogr. **11**, 102 (1978). https://doi.org/10.1107/S0021889878012844

50. L. Randolph, M. Banjafar, T.R. Preston, T. Yabuuchi, M. Makita, N.P. Dover, C. Rödel, S. Göde, Y. Inubushi, G. Jakob, J. Kaa, A. Kon, J.K. Koga, D. Ksenzov, T. Matsuoka, M. Nishiuchi, M. Paulus, F. Schon, K. Sueda, Y. Sentoku, T. Togashi, M. Vafaee-Khanjani, M. Bussmann, T.E. Cowan, M. Kläui, C. Fortmann-Grote, A.P. Mancuso, T. Kluge, C. Gutt, M. Nakatsutsumi Phys. Rev. Research **4**, 033038 (2022). https://doi.org/10.1103/PhysRevResearch.4.033038

51. W. Roseker, S.O. Hruszkewycz, F. Lehmkühler, M. Walther, H. Schulte-Schrepping, S. Lee, T. Osaka, L. Strüder, R. Hartmann, M. Sikorski, S. Song, A. Robert, P.H. Fuoss, M. Sutton, G.B. Stephenson, G. Grübel, Nat. Commun. **9**, 1704 (2018). https://doi.org/10.1038/s41467-018-04178-9

52. Y. Sun, G. Carini, M. Chollet, F.J. Decker, M. Dunne, P. Fuoss, S.O. Hruszkewycz, T.J. Lane, K. Nakahara, S. Nelson, A. Robert, T. Sato, S. Song, G.B. Stephenson, M. Sutton, T.B. Van Driel, C. Weninger, D. Zhu, Phys. Rev. Lett. **127**, 058001 (2021). https://doi.org/10.1103/PhysRevLett.127.058001